PHYSICAL REVIEW C VOLUME 52, NUMBER 1 JULY 1995

Surface properties of Cs isotopes

S. Yoshida, S.K. Patra, and N. Takigawa
Department of Physics, Faculty of Science, Tohoku University, 980-77 Sendai, Japan

C.R. Praharaj
Institute of Physics, Bhubaneswar-751 005, India

(Received 17 March 1995)

The neutron-skin property of Cs isotopes is studied by the deformed relativistic mean-field and spherical nonrelativistic Hartree-Fock theories. We predict a sizable neutron-skin ratio for the isotopes not only near the neutron-drip line, but also far inside, where experimental studies could be done with the present-day experimental facilities. We also show that the surface diffuseness of the neutron distribution increases with the neutron number.

PACS number(s): 21.10.Gv, 21.10.Dr, 21.60.Jz, 27.60.+j

In the past several years the radioactive beams in various laboratories in the world have provided much intriguing experimental information on the structure and reactions of nuclei near the proton and neutron drip lines [1,2], and the results are attracting much theoretical attention. The existence of neutron halos in some of the nuclei on the neutron drip line is by now well established. Extensive experimental as well as theoretical studies are now going on to clarify the effects of the neutron halo on the fusion cross section in heavy-ion collisions when one of the halo nuclei is used as the projectile [3–9]. The existence of the proton halo is more subtle. For example, there are different interpretations [10,11] of the large quadrupole moment of ^{8}B, which is claimed to have a proton halo [12]. The discovery of new isotopes near the proton drip line by the MSU group [13] opens a new path of nucleosynthesis by rapid proton (rp) capture [14]. Similarly, the discovery of new neutron-rich nuclei near the neutron drip line is important to understand the rapid neutron (rn) capture process in accreting stellar systems [15].

In this paper, we discuss the change of nuclear structure along the isotope chain of Cs. We choose Cs isotopes, because unstable isotope beams of alkali elements are relatively easy to be produced by an experimental facility of the ISOLDE type. We discuss the rms radii of the proton and the neutron distributions, nuclear shape, the two-neutron separation energy, and the density profile. We discuss in some detail the skin properties of unstable isotopes, and the change of surface diffuseness along the isotope chain. These properties are of interest not only in themselves, but also in connection with reactions induced by unstable nuclei, because the fusion and the multinucleon transfer reactions induced by unstable nuclei, for example, will be strongly influenced by their surface properties [5].

We study the structure of Cs isotopes based on the deformed nonlinear relativistic mean-field (RMF) model. We also compare the results with those of spherical nonrelativistic Skyrme-Hartree-Fock (SHF) calculations. The relativistic mean-field model has the advantage that, with the proper relativistic kinematics and with the mesons and their properties already known or fixed from the properties of a small number of nuclei [16], the method gives excellent results for the binding energies, root mean square (rms) radii, quadrupole and hexadecupole deformations, and other nuclear properties, not only of spherical nuclei, but also of deformed nuclei [16–22]. The same parameter set also well describes the properties of nuclear matter. One of the major attractive features of the RMF approach is that the spin-orbit interaction and the associated nuclear shell structure automatically arise from meson-nucleon interaction [20–22]. The inclusion of ρ mesons takes care of the neutron-proton asymmetry. We can thus expect that the RMF calculations provide useful information about the structure of nuclei far from the stability line, including those near the neutron and the proton drip lines.

On the other hand, the Skyrme-Hartree-Fock [23,24] calculation is a well advanced and successful approach to a variety of nuclear phenomena, including deformation, superheavy nuclei, vibrations, and heavy-ion collisions [25]. It also well describes nuclear matter properties and giant resonances, isobaric analogue states, and low-lying particle-hole excitations. A detailed description of the SHF calculations can be found in [24,26].

However, we have to be aware of the fact that the theoretical results delicately depend on the details of the input parameters, both in the relativistic and in the nonrelativistic calculations. The most commonly used parameter sets NL1 and NL2 in the RMF theory predict too large neutron radii compared with the experimental values [27]. This shortcoming may arise from the large value of the asymmetry energy in these sets, which is about 44 MeV. Sharma *et al.* [27] introduced a new parameter set by modifying the NL1 set. This new parameter set has been used for calculating a series of nuclei including deformed and highly exotic nuclei on both sides of the stability lines. It is more successful in reproducing the experimental data of the rms radii, deformations, and the binding energy of unstable nuclei. This new set of parameters is called the NL-SH set, and

0556-2813/95/52(1)/157(7)/$06.00

its values and nuclear matter properties can be found in Ref. [27]. In the present work, we use this set in the relativistic calculations. On the other hand, Giai and Sagawa [28] improved the original Skyrme-Hartree-Fock calculations which used forces with too high incompressibility by introducing a weaker density dependence. They also introduced the spin-exchange properties in the velocity-dependent parts of the interaction. We use the improved parameter set of Giai and Sagawa, the SGII set [28], in our nonrelativistic calculations.

We solve the relativistic Hartree equations by a self-consistent iterative method [17] based on an expansion in the basis of deformed axially symmetric harmonic oscillator wave functions. The initial deformation parameter β_0 for the basis expansion is taken from [29]. We truncate the harmonic oscillator bases at the maximum oscillator quanta $N_{\max} = 12$ for both bosons and fermions. We have checked that the results do not change on increasing $N_{\max}$. We ignored the spatial components of the vector meson fields, which may become finite because of the breaking of time-reversal symmetry [17]. The details of the numerical procedure for the nonrelativistic Hartree-Fock calculations are given in Refs. [24,30]. In both relativistic and nonrelativistic calculations, the pairing interaction has been treated in the BCS theory assuming a constant gap given in Ref. [29] except for the magic nuclei ^{137}Cs and ^{181}Cs, for which we set the gap parameter for neutrons to be zero.

TABLE I. Root mean square radii of the neutron and the proton distributions obtained by various parameter sets in both the RMF and nonrelativistic SHF models. The last column (Expt.) are experimental data of 800 MeV polarized proton scattering [31].

Nucleus	NL-SH	NL1	NL2	SGII	SkM*	SIII	Expt.
^{40}Ca							
r_n	3.340	3.359	3.340	3.326	3.377	3.357	3.491
r_p	3.399	3.405	3.391	3.375	3.427	3.402	3.392
^{48}Ca							
r_n	3.614	3.644	3.667	3.574	3.616	3.607	3.625
r_p	3.383	3.396	3.359	3.420	3.449	3.459	3.396
^{58}Ni							
r_n	3.692	3.686	3.731	3.700	3.721	3.744	3.700
r_p	3.682	3.637	3.719	3.708	3.721	3.748	3.686
^{64}Ni							
r_n	3.908	3.950	3.936	3.873	3.908	3.913	3.912
r_p	3.745	3.726	3.761	3.775	3.785	3.821	3.745
^{90}Zr							
r_n	4.296	4.351	4.331	4.260	4.290	4.309	4.289
r_p	4.189	4.215	4.195	4.205	4.225	4.256	4.204
^{116}Sn							
r_n	4.696	4.752	4.726	4.638	4.670	4.688	4.692
r_p	4.537	4.546	4.541	4.556	4.562	4.611	4.546
^{124}Sn							
r_n	4.844	4.920	4.888	4.761	4.798	4.807	4.851
r_p	4.588	4.606	4.595	4.612	4.618	4.669	4.599
^{140}Ce							
r_n	5.004	5.072	5.036	4.929	4.955	4.978	4.971
r_p	4.808	4.835	4.813	4.831	4.831	4.887	
^{208}Pb							
r_n	5.710	5.789	5.755	5.590	5.628	5.650	5.593
r_p	5.447	5.476	5.453	5.458	5.460	5.528	5.453

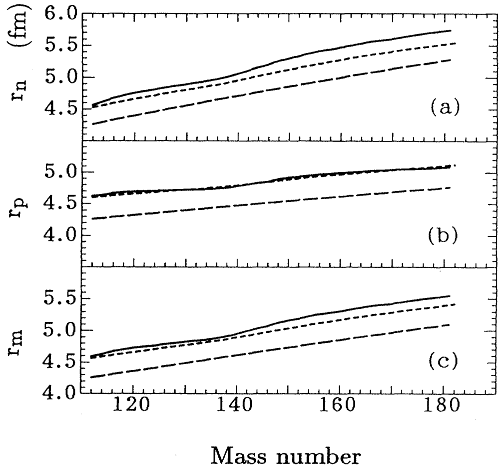

FIG. 1. The rms radii of (a) the neutron, (b) the proton, and (c) the matter distributions as functions of the mass number for Cs isotopes. The solid and the short dashed lines are the results of the RMF and the nonrelativistic SHF calculations, respectively. The long dashed line is the result of Myers' formula given in [33].

We now discuss the results of our numerical calculations. We first focus our attention on the radii of the neutron and proton distributions. In order to confirm that the NL-SH and SGII parameter sets are adequate, we compare in Table I the results of our calculations of the radii of the neutron and the proton distributions for some known nuclei calculated by several parameter sets. The table shows that all the parameter sets in both RMF and SHF calculations excellently reproduce both the experimental neutron and proton distribution radii r_n and r_p for known stable nuclei. As we mentioned before, however, NL1 and NL2 overestimate the known neutron distribution radius for unstable nuclei. Also, the experimental data of the quadrupole moments of unstable W isotopes agree better with the results of the NL-SH set rather than those of the NL1 set [32].

In Fig. 1, we plot the rms radii of neutron (r_n), proton (r_p), and matter (r_m) distributions as functions of the mass number for Cs isotopes. The rms radii of the proton distribution are almost the same in the RMF (the solid line) and SHF calculations (the short dashed line). The rms radii of the neutron and the matter distributions are predicted to be slightly larger for all isotopes in the relativistic calculations using NL-SH than in the nonrelativistic calculations assuming SG-II. This subtle difference depends, however, on the choice of forces as we see in Table I. The figure contains also r_n, r_p, and r_m calculated based on the analytic expressions of Myers [33] (the long dashed lines). We see that Myers' formulas give systematically smaller radii compared with the results of both the relativistic and nonrelativistic calculations.

Figure 2 shows the results of our relativistic and non-

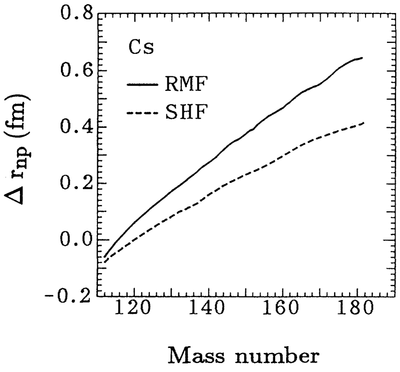

FIG. 2. Difference between the rms radii of the neutron and the proton distributions $\triangle r_{np}$ as a function of the mass number. The solid and the dashed lines are the results of the RMF and SHF models, respectively.

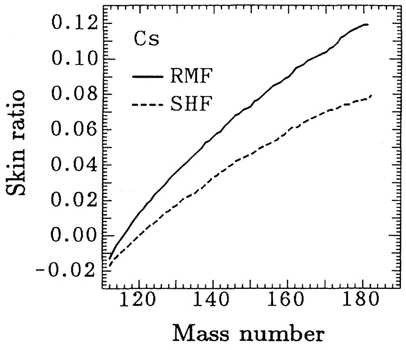

FIG. 4. Neutron-skin ratio $ns = 2(r_n - r_p)/(r_n + r_p)$ as a function of the mass number for Cs isotopes. The solid and the dashed lines are the results of the RMF and nonrelativistic SHF models, respectively.

relativistic calculations for the difference between the neutron and the proton distribution radii $\triangle r_{np}$, defined by $\triangle r_{np} = r_n - r_p$, as a function of the mass number. The NL-SH RMF calculations predict constantly larger values of $\triangle r_{np}$ than the SG-II SHF calculations. One notices that the radius of the proton distribution is larger than that of the neutron distribution for proton-rich isotopes. This difference is, however, very small. This indicates that there is no significant proton skin for these large Z nuclei. This is due to a large Coulomb repulsion. With increasing neutron number, the radius of the neutron distribution increases faster than that of the proton distribution leading to the neutron skin as we discuss shortly.

In Fig. 3, we plot the quadrupole deformation parameter β as a function of the mass number. As we expect, the shape is almost spherical when the neutron number is close to a magic number 82 and 126.

The existence of a neutron skin or a neutron halo is an intriguing question concerning the structure of unstable nuclei [34,35]. In this connection, we present in Fig. 4 the results shown in Fig. 2 in the form of the neutron skin. Among various definitions of the neutron skin, we use the ratio $ns = \frac{2(r_n - r_p)}{(r_n + r_p)}$ following Krasznaborkay *et al.* [35]. We refer to ^{208}Pb as the standard nucleus, and judge that a certain nucleus has a neutron skin if its ns value is larger than that of ^{208}Pb. The value of ns for ^{208}Pb is predicted to be 0.05 and 0.01 in the RMF and SHF calculations, respectively. Figure 4 shows that the skin formation starts beyond $A > 136$ for Cs isotopes. Though the RMF calculations give larger skin ratio than the SHF calculations, both of them predict that the neutron skin increases with increasing neutron number. The results of our nonrelativistic calculations agree with the results in [34], though another definition of the neutron skin is used there. In our calculations, the maximum skin ratio is 0.12 and 0.08 for the drip line nuclei ^{181}Cs and ^{182}Cs in the RMF and SHF calculations, respectively.

The two-neutron separation energy S_{2n} plays a crucial role in order to form the neutron halo in drip line nuclei. It will also play an important role in forming a neutron skin near the neutron drip line. The two-neutron separation energy is shown in Fig. 5 as a function of the mass number. The solid dots and the solid and dashed lines denote the experimental two-neutron separation energy [36] and that obtained by the RMF and the nonrelativistic calculations, respectively. The RMF calculations agree fairly well with the experimental data of S_{2n}, though they

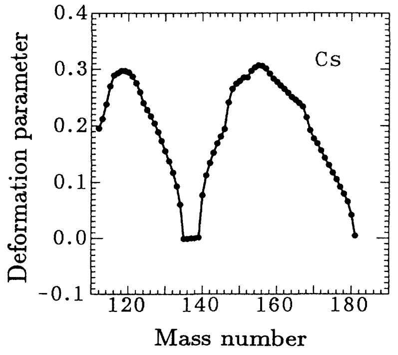

FIG. 3. Quadrupole deformation parameter as a function of the mass number. The results of relativistic calculations are shown.

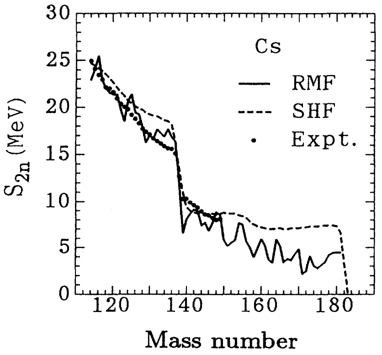

FIG. 5. Two-neutron separation energy (S_{2n}) in RMF (the solid line) and nonrelativistic SHF (the dashed line) models. The dots are the experimental values taken from Ref. [36].

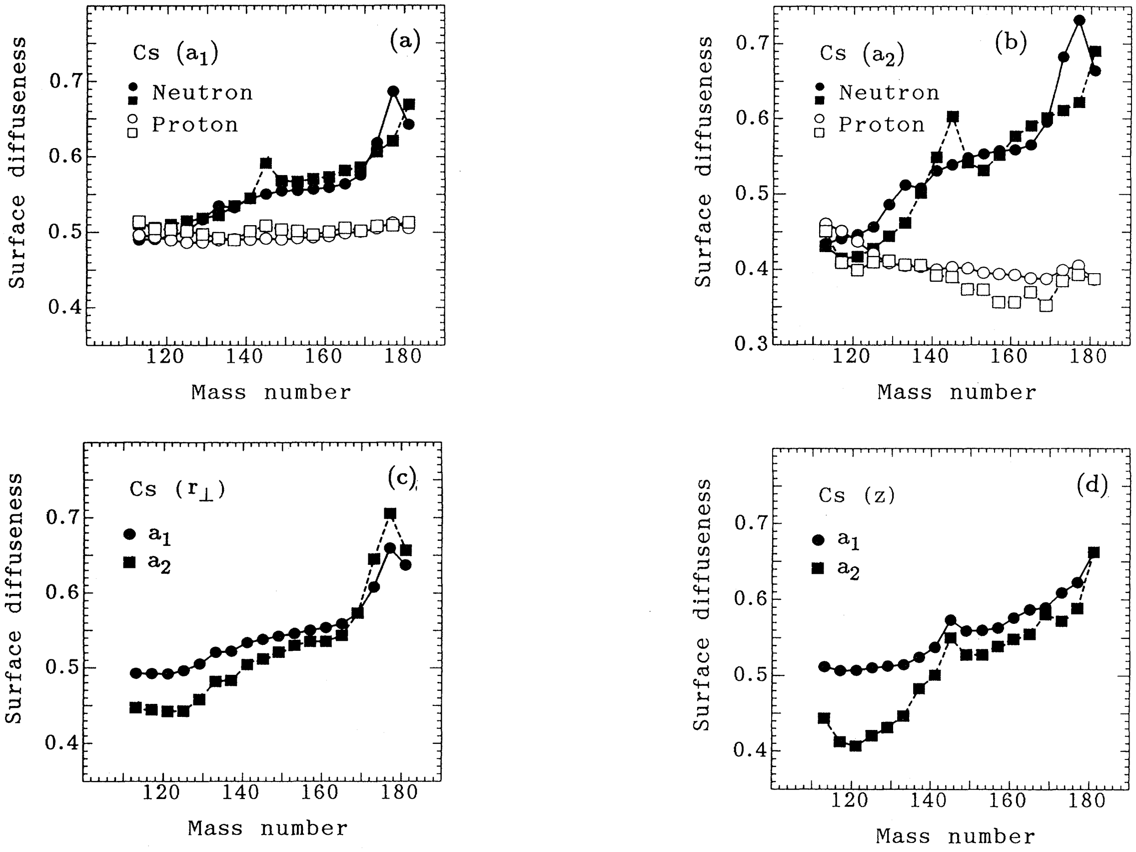

FIG. 6. (a) Inner surface diffuseness parameter a_1 as a function of the mass number. The closed and the open symbols refer to neutrons and protons, respectively. The squares and the circles are for the direction along the axially symmetric axis and for the perpendicular direction, respectively. (b) The same as (a), but for the outer surface diffuseness parameter a_2. (c) Comparison of the inner and the outer surface diffuseness parameters a_1 and a_2 in the direction along the axially symmetric axis. We used the sum of the neutron and the proton densities. (d) The same as (c), but along the direction perpendicular to the axially symmetric axis.

show some staggering, which is probably due to the ignorance of the spatial component of the vector meson fields in our calculations. On the other hand, nonrelativistic calculations systematically give slightly larger S_{2n} for almost all Cs isotopes. We observe that S_{2n} drastically decreases beyond mass number $A = 137$. This is the mass number where neutrons start to fill the next major shell. As we see in Fig. 4, this is also the transitional region, where a neutron skin starts to be formed.

We now move to the problem of the surface diffuseness. We fitted the density profile obtained by either relativistic or nonrelativistic calculations by introducing different functions for the inner and the outer regions,

$$\rho(r) = \begin{cases} \dfrac{\rho_1}{1 + e^{(r-R_1)/a_1}} & (r < R') \\ \rho_2 e^{-r/a_2} & (r > R'), \end{cases} \tag{1}$$

where ρ_1, ρ_2, R_1, a_1, and a_2 are fitting parameters. R' was chosen to be the radius where the density becomes 10% of the central density. The reason why we introduce different functions for the inner and the outer regions is because the properties of the nuclear surface in the region of extremely small density and in the region with moderate density will be governed by different physical quantities. For example, the surface diffuseness in the external region will be related to the separation energy of the last nucleons, whereas that in the region with moderate density will be governed by the nuclear incompressibility and the effective mass of the nucleons [37–39].

Figures 6(a) and 6(b) show the inner and outer surface diffuseness parameters a_1 and a_2 for protons (open symbols) and neutrons (closed symbols) separately as functions of the mass number. Each ΔN=4 isotope with even neutron number is shown. The squares and the circles are the surface diffuseness in the z direction, i.e., in the direction of the axially symmetric axis, and that in the perpendicular direction, respectively. We observe that the surface diffuseness of the neutron distribution increases with increasing neutron number, while that of the proton distribution stays almost constant. Figures 6(c) and 6(d) compare a_1 and a_2 in two directions. Here, we used the total density. We observe that a_1 is larger than a_2 for almost all isotopes except for nuclei close to the neutron drip line for the direction perpendicular to the axially symmetric axis. These trends hold irrespective of the choice of the force. The absolute value of the surface diffuseness, on the other hand, strongly depends on the choice of the force. For example, NL1, whose incompressibility is roughly half that of NL-SH, gives much larger surface diffuseness than NL-SH. Similarly, the magnitude of the surface diffuseness depends on the choice of forces in nonrelativistic Skyrme-Hartree-Fock calculations through their different properties regarding the incompressibility and the effective mass. Note that in this case the inner surface diffuseness parameter a_1 for nuclear matter is related to the incompressibility K and the force parameters t_1 and t_2 as [38]

$$a_1 = \frac{2}{3}\left[\frac{9\rho_0}{32K}\left\{9t_1 - t_2(5+4x_2)\right\} + \frac{\hbar^2}{4mK}\right]^{\frac{1}{2}} , \qquad (2)$$

where ρ_0 and x_2 are the central density and an exchange parameter in the Skyrme force, respectively.

Note that t_1 and t_2 are related to the effective mass, though the latter depends on t_1 and t_2 in a different combination from that for a_1 given in Eq. (2):

$$\frac{\hbar^2}{2m^*(r)} = \frac{\hbar^2}{2m(r)} + \frac{1}{16}\left\{3t_1 + t_2\left(5+4x_2\right)\right\}\rho(r) . \qquad (3)$$

The increase of the surface diffuseness with increasing number of neutron excess could be related to the decrease of the incompressibility due to the symmetry term [40–43].

It would be an interesting problem to derive similar equations to Eqs. (2) and (3) for the parameters in RMF calculations. To this end, one could use the relationships between the Skyrme parameters t_1 and t_2 and the parameters in the RMF theory, which have been obtained in [44]. We found, however, that these relationships give too large surface diffuseness compared with that obtained by fitting the density provided by the numerical calculations. This could be related to the fact that they give much larger effective mass than that given by $m^* = m - g_S \cdot \phi$, ϕ being the scalar field. These puzzles should be resolved in the future.

Concerning the surface diffuseness in the outer region, Fig. 6(b) shows that a_2 for neutrons in the direction of the axially symmetric axis (closed squares) increases like a step function at around mass number 137, and then gradually increases towards the neutron drip line, though there exists a local minimum at A=152. This noticeable change around the mass number 137 reflects the drastic decrease of the two-neutron separation energy around that nucleus (see Fig. 5). Also, the mass formula of Tachibana *et al.* [45] suggests that the neutron separation energy suddenly decreases at nearly the same mass number. These indicate that the surface diffuseness in the outer region is indeed related to the separation energy of the last nucleons. Notice that the solid squares and the solid circles in Figs. 6(a) and 6(b) coincide at A=137. This has to be so, because the isotope with A=137 is almost spherical due to the magic neutron number N=82. The disagreement of the solid circle and the solid square at the other magic isotope the A=181 will be because the deformation parameter is not completely zero, but finite,

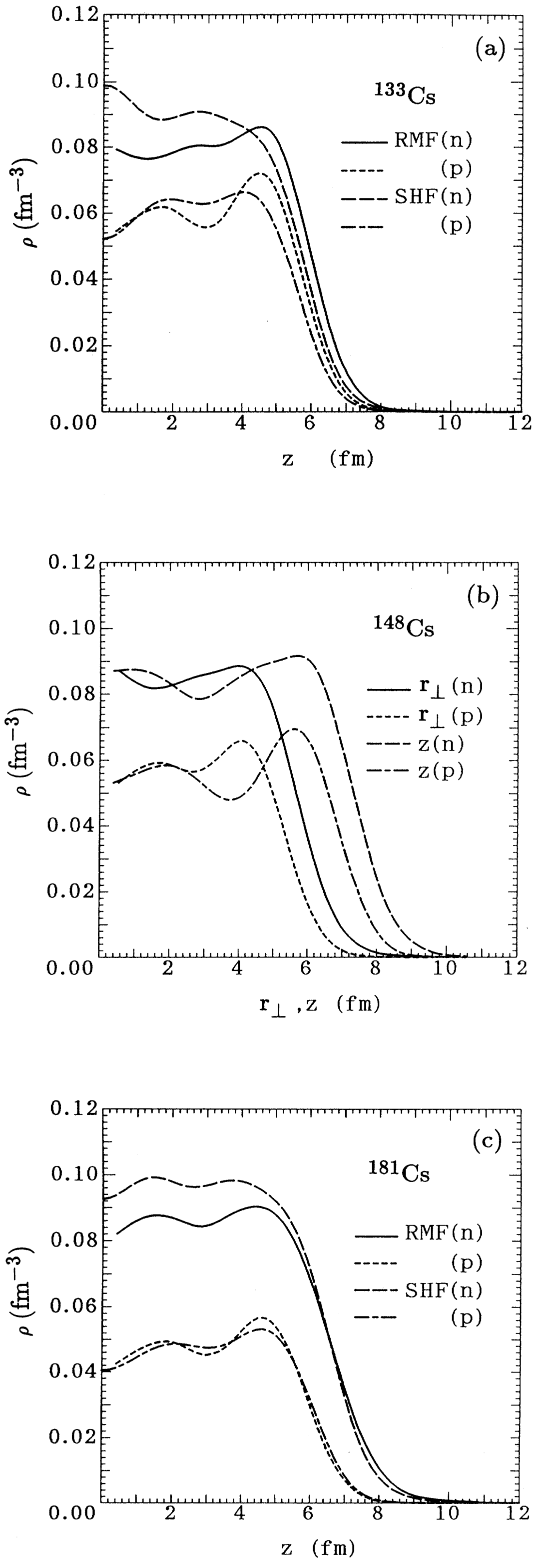

FIG. 7. (a) Density distributions of the neutrons and protons in ^{133}Cs along the axially symmetric axis. (b) Density distributions of the neutrons and protons in ^{148}Cs along the axially symmetric and the perpendicular axes. Only the results of relativistic calculations are shown. (c) The same as (a), but for ^{181}Cs.

i.e., $\beta = 0.007$ for A=181. On the other hand $\beta = 0.0002$ for the isotope A=137. The octupole moment is also more than two times larger in the A=181 isotope than in the A=137 isotope. In these senses, the isotope with mass number 181 is less magic than that with A=137.

The change of the radii and the surface properties discussed above can be visualized by plotting the density profile. Figure 7 shows the density distributions of neutrons and protons for three representative isotopes, ^{133}Cs, ^{148}Cs, and ^{181}Cs, obtained in both the RMF and SHF calculations. ^{133}Cs is the unique stable nucleus among the Cs isotopes. ^{181}Cs resides at the neutron drip line, in the case of RMF calculations. We chose ^{148}Cs as the example of unstable nuclei, because experimental study could be feasible up to this isotope in the present experimental facilities. Figure 7(a) shows the neutron and the proton densities of ^{133}Cs along the axially symmetric axis. The results of both relativistic and nonrelativistic calculations are shown. The density profile along the perpendicular axis looks similar. Figure 7(b) shows the neutron and the proton densities for ^{148}Cs along the axially symmetric and the perpendicular axes, respectively. Only the results of relativistic calculations are shown. Figure 7(c) shows the density distributions of ^{181}Cs along the axially symmetric axis obtained by the relativistic and nonrelativistic calculations. Since this nucleus is almost spherical, the density distributions along the perpendicular axis are almost the same. Comparison of these figures clearly demonstrates that the neutron distribution extends more than the proton distribution as the number of neutrons increases, thus forming a neutron skin. Figure 7(b) shows that a sizable neutron skin exists in both directions already for ^{148}Cs. Figures 7(a) and 7(c) show that relativistic and nonrelativistic calculations give qualitatively similar behavior regarding the surface properties.

In summary, we discussed the density and the surface properties of Cs isotopes based on deformed RMF and spherical nonrelativistic SHF calculations. Our calculations predict a large neutron skin with skin ratio $ns = 0.12$ and $ns = 0.08$ for the nuclei on the neutron drip line, ^{181}Cs and ^{182}Cs in RMF and SHF calculations, respectively. An interesting thing is that a sizable neutron skin is predicted already for nuclei far inside the drip line, which could be studied by the existing experimental facilities. On the other hand, no proton skin was predicted for all isotopes including that on the proton drip line, i.e., ^{112}Cs. Our calculations predict that the neutron skin and the surface diffuseness of the neutron distribution increase with increasing neutron number. We are now studying how these properties affect heavy-ion reactions, such as fusion reactions at energies below the Coulomb barrier and multinucleon transfer reactions during deep inelastic heavy-ion collisions, when one of the neutron-rich nuclei is used as the projectile [46]. The results will be reported in separate papers.

We would like to thank Professor Nguyen Van Giai, Professor H. Sagawa, Professor H. Floard, Professor N. Tajima, and Professor T. Shinozuka for useful discussions. One of the authors (S.K.P.) is grateful to the Japanese Government for financial support. This work is supported by the Grant-in-Aid for General Scientific Research, Contract No. 06640368, from the Japanese Ministry of Education, Science and Culture.

---

[1] I. Tanihata *et al.*, Phys. Rev. Lett. **55**, 2676 (1985).

[2] W. Mittig *et al.*, Phys. Rev. Lett. **59**, 1889 (1987); M.G. Saint-Laurent *et al.*, Z. Phys. A **332**, 457 (1989).

[3] N. Takigawa and H. Sagawa, Phys. Lett. B **265**, 23 (1991).

[4] N. Takigawa, M. Kuratani, and H. Sagawa, Phys. Rev. C **47**, R2470 (1993).

[5] N. Takigawa, M. Kuratani, S. Yoshida, H. Sagawa, and M. Abe, in *Proceedings of the Third International Conference on Radioactive Nuclear Beams*, East Lansing, Michigan, 1993, edited by D.J. Morrissey (Editions Frontieres, Gif-sur-Yvette, 1993), p. 521.

[6] M.S. Hussein and A.F.R. de Toledo Pisa, Phys. Rev. Lett. **72**, 2693 (1994).

[7] C.H. Dasso and A. Vitturi, Phys. Rev. C **50**, R12 (1994).

[8] K. Kim, T. Otsuka, and M. Tohyama, Phys. Rev. C **50**, R566 (1994).

[9] A. Yoshida *et al.*, in *Proceedings of the International Workshop on Heavy-Ion Fusion: Exploring the Variety of Nuclear Properties*, Padova, 1994 (World Scientific, Singapore, 1994) p. 312; V. Fekou-Youmbi *et al.*, *ibid.* p. 305.

[10] H. Kitagawa and H. Sagawa, Phys. Lett. B **299**, 1 (1993).

[11] H. Nakada and T. Otsuka, Phys. Rev. C **49**, 886 (1994).

[12] T. Minamisono *et al.*, Phys. Rev. Lett. **69**, 2058 (1992).

[13] M.F. Mohar *et al.*, Phys. Rev. Lett. **66**, 1571 (1991).

[14] S.K. Patra and C.R. Praharaj, Europhys. Lett. **20**, 87 (1992).

[15] E.M. Burbidge, G.R. Burbidge, W.A. Fowler, and F. Hoyle, Rev. Mod. Phys. **29**, 547 (1957); D.D. Clayton and S.E. Woosley, *ibid.* **46**, 755 (1974).

[16] P.G. Reinhard, M. Rufa, J. Maruhn, W. Greiner, and J. Friedrich, Z. Phys. A **323**, 13 (1986).

[17] Y.K. Gambhir, P. Ring, and A. Thimet, Ann. Phys. (N.Y.) **198**, 132 (1990).

[18] L.S. Celenza *et al.*, Phys. Rev. C **41**, 1768 (1990); Sara Cruz-barrios *et al., ibid.* **43**, 181 (1991); R.J. Furnstahl, C.E. Price, and G.E. Walker *ibid.* **36**, 2590 (1987); R. Brockman, *ibid.* **18**, 1510 (1978).

[19] B.D. Serot and J.D. Walecka, Adv. Nucl. Phys. **16**, 1 (1986).

[20] C.J. Horowitz and B.D. Serot, Nucl. Phys. **A368**, 503 (1981).

[21] B.D. Serot, Rep. Prog. Phys. **55**, 1855 (1992); P.G. Reinhard, Rep. Prog. Phys. **52**, 439 (1989).

[22] S.K. Patra and C.R. Praharaj, Phys. Rev. C **44**, 2552 (1991).

[23] T.H.R. Skyrme, Nucl. Phys. **9**, 615 (1959).

[24] D. Vautherin and D.M. Brink, Phys. Rev. C **5**, 626 (1972).

[25] P. Quentin and H. Flocard, Annu. Rev. Nucl. Part. Sci. **28**, 523 (1978); S.J. Krieger, in *Proceedings of the International Symposium on Time-Dependent Hartree-Fock and Beyond*, Bad Honnef, 1982, edited by K. Goeke and P.-G. Reinhard, Lecture Notes in Physics, Vol. 171 (Springer-Verlag, Berlin, 1982), p. 1.

[26] M. Beiner, H. Flocard, Nguyen Van Giai, and P. Quentin, Nucl. Phys. **A238**, 29 (1975).

[27] M.M. Sharma, M.A. Nagarajan, and P. Ring, Phys. Lett. B **312**, 377 (1993).

[28] Nguyen Van Giai and H. Sagawa, Phys. Lett. **106B**, 379 (1981).

[29] P. Möller, W.D. Myers, W.J. Swiatecki, and J. Treiner, Report No. LBL-22686.

[30] J. Friedrich and P.-G. Reinhard, Phys. Rev. C **33**, 335 (1986).

[31] C.J. Batty, E. Friedman, H.J. Gils, and H. Rebel, Adv. Nucl. Phys. **19**, 1 (1989).

[32] M. Fujita, M.S. thesis, Tohoku University, 1995.

[33] W.D. Myers, Phys. Lett. **30B**, 451 (1969).

[34] N. Fukunishi, T. Otsuka, and I. Tanihata, Phys. Rev. C **48**, 1648 (1993).

[35] A. Krasznahorkay *et al.*, Phys. Rev. Lett. **66**, 1287 (1991); M.M. Sharma and P. Ring, Phys. Rev. C **45**, 2514 (1992); I. Tanihata, D. Hirata, T. Kobayashi, S. Shimoura, K. Sugimoto, and H. Toki, Phys. Lett. B **289**, 261 (1992).

[36] G. Audi and A. H. Wapstra, Nucl. Phys. **A565**, 1 (1993).

[37] J.P. Blaizot, Phys. Rep. **64**, 171 (1980).

[38] M. Brack, C. Guet, and H. B. Håkansson, Phys. Rep. **123**, 275 (1985).

[39] O. Bohigas, X. Campi, H. Krivine, and J. Treiner, Phys. Lett. **64B**, 381 (1976).

[40] J.P. Blaizot and B. Grammaticos, Nucl. Phys. **A355**, 115 (1981).

[41] J. Treiner, H. Krivine, O. Bohigas, and J. Martorell, Nucl. Phys. **A371** 253 (1981).

[42] M.M. Sharma, W. Stocker, P. Gleissl, and M. Brack, Nucl. Phys. **A504**, 337 (1989).

[43] J.M. Pearson, Phys. Lett. B **271**, 12 (1991).

[44] M. Thies, Phys. Lett. **166B**, 23 (1986).

[45] T. Tachibana, M. Uno, M. Yamada, and S. Yamada, At. Data Nucl. Data Tables **39**, 251 (1988).

[46] N. Takigawa, S. Yoshida, K. Hagino, and S.K. Patra, Nucl. Phys. A **588**, 91c (1995).